Colloid Polym Sci (2013) 291:1729–1740
DOI 10.1007/s00396-013-2908-y

ORIGINAL CONTRIBUTION

Effect of molecular interactions on the performance of poly (isobutylene-*co*-isoprene)/graphene and clay nanocomposites

Kishor Kumar Sadasivuni · Allisson Saiter · Nicolas Gautier · Sabu Thomas · Yves Grohens

Received: 13 October 2012 / Revised: 6 January 2013 / Accepted: 16 January 2013 / Published online: 8 February 2013

Abstract Poly(isobutylene-*co*-isoprene) (IIR)/graphene and cloisite10A nanocomposites were prepared successfully and the resulting mechanical, rheological and barrier properties were carefully evaluated and compared. Chemical treatments like maleic anhydride grafting were used to improve the dispersion of the clay in the IIR matrix. Blends with different loading (20, 40, 60, and 80 %) of maleic anhydride grafted poly(isobutylene-*co*-isoprene) (MA-g-IIR) and IIR were made to maintain a balance between the beneficial polarity induced by MA grafting and the inevitable decrease in molecular weight (due to chain scission) induced by the free radical grafting process. The highest moduli, tensile strength and elongation at break were achieved in the case of a 60:40 ratio of MA-g-IIR (grafting degree 0.75)/IIR mixture with 5 phr of cloisite 10A. IIR/graphene nanocomposites exhibited higher reinforcement (Young's moduli) and lower gas permeability compared to the optimized clay nanocomposites with same weight percentage. The filler–elastomer and filler–filler interactions deduced from rheology, stress relaxation and Payne effect experiments emphasize the reinforcing ability in IIR/graphene and MA-g-IIR/clay. XRD, SEM and TEM results further substantiated the results from the obtained micro structure of the nanocomposites. The improved performances of IIR/MA-g-IIR/clay and IIR/graphene were successfully correlated with interactions between the filler platelets and elastomer chains occurring in the nanocomposites.

Keywords Elastomer nanocomposites · Maleic anhydride grafting · Interfaces · Nonlinear behavior · Stress relaxation · Payne effect

K. K. Sadasivuni · Y. Grohens
LIMATB Laboratory, Université de Bretagne Sud, rue St Maudé, 56100 Lorient, France

K. K. Sadasivuni · S. Thomas (✉)
School of Chemical Sciences, Mahatma Gandhi University, Kottayam 686560 Kerala, India
e-mail: sabupolymer@yahoo.com

A. Saiter
AMME-LECAP, EA 4528 International Laboratory, Institute of Material Research FED4114, Université de Rouen, Faculté des Sciences, Avenue de l'Université BP 12, 76801 Saint Etienne du Rouvray, France

N. Gautier
Institut des Matériaux Jean Rouxel UMR 6502, Centre de Microcaractérisation, 2 rue de la Houssinière, B.P. 32229, 44322 Nantes Cedex 3, France

Introduction

Polymer nanocomposites (PNCs) have become one of the most significant subjects of research since from 1984, when the Toyota Research Group of Japan reported the development of PA6–clay nanocomposites for the first time [1]. The high aspect ratio, large surface area and substantial reinforcement of nanoparticles compared to their conventional counterparts made researchers to put great efforts on the development, characterization and modeling of PNCs [2, 3]. However, the key issue in manufacturing nanocomposites is to obtain a complete dispersion of filler in the matrix and maximum interfacial compatibility. For 2D nano sheets, the individual layers have much higher aspect ratio than typical microscopic aggregates, which have to be exfoliated to yield high performance nanocomposites [4]. Nanoclays impart outstanding mechanical and permeability properties to elastomer nanocomposites due to their large interfacial area and attractive interactions per unit volume with the matrix [2, 5, 6]. It is reported that the dispersion state of the organoclay in a rubber matrix is mainly influenced by the nature of aggregated platelets [7–9], compounding

conditions [10, 11] (shear rate and temperature) and polarity of the rubber matrix [12, 13]. Rubbers exhibit high melt viscosities during melt mixing because of their high molecular weight and this paves the path for the generation of high shear stresses for shearing and peeling apart of the silicate layers [14]. In addition to melt compounding, several other techniques like in situ polymerization [15, 16], solvent-assisted mixing [17], and emulsion compounding, are also used to disperse fillers in rubber matrices at a nano-scopic scale.

Apart from the clay nanocomposites, great interest has been laid on rubber/graphene nanocomposites to get improvement in mechanical, electrical and permeability properties [15, 17–20]. Graphene is an atomically thick two dimensional sheet of sp^2-bonded carbon atoms (2-D) arranged like a honeycomb structure with ultra-high specific surface area (theoretical limit ~2,630 m^2/g) [21]. Moreover, outstanding mechanical, electrical, thermal and gas impermeability properties were also demonstrated [22–24] for this material. At low concentrations, barrier properties of graphene sheets are ~25–130 times higher than that of clay nano fillers [25] and more effective (by a factor of 1 order of magnitude or higher) than predicted by the modified Nielsen, Cussler and Bharadwaj theories [26–28]. However, to fulfill these expectations, the fillers have to be uniformly dispersed in the elastomer matrix without any agglomeration. Huiqin et al. [17] reported well-dispersed modified graphene (MG) in IIR (poly(isobutylene-*co*-isoprene)) composites through solution mixing process, with dramatically enhanced mechanical properties. Yanhu et al. [15] used an ultrasonically assisted latex mixing and in situ reduction (ULMR) process to prepare natural rubber latex (NRL)/graphene composites. The effect of functionalized graphene on natural rubber (NR) and styrene butadiene rubber (SBR) matrices are demonstrated by Prud'homme et al. [19]. Xin et al. [20] explained the reinforcement of hydrogenated carboxylated nitrile–butadiene rubber (HXNBR) with exfoliated graphene oxide (GO). The strong interfacial interactions between the oxygen-containing functional groups on the surfaces of GO nano sheets and the carboxyl groups in HXNBR improved the mechanical properties, even at very low level of GO loading.

IIR is a copolymer of isobutylene (97–98 %) and a small amount of isoprene (2–3 %). Since its commercialization in 1943, the rubber finds enormous applications in many areas because of its excellent properties such as impermeability/air retention, weathering resistance, ozone resistance, vibration dampening, and sealing efficiency. It has good flexing properties as well, resulting from the low levels of unsaturation between long polyisobutylene segments [29–32]. This synthetic rubber is used in a wide range of applications such as inner tubes, tyre liners, curing bladders, air springs, sealants, gas pipe coating and gaskets, air conditioner hoses, cable insulations, jacketing, roof membranes and sporting goods [29, 33, 34]. However, various nano fillers and other additives are added to IIR to improve its performances further. IIR/clay nanocomposites are difficult to prepare because of the hydrophobicity of IIR and its poor interaction with clay silicate layers [35]. However, both solution and melt mixed samples having similar intercalated structures are reported, [36–40] with better mechanical and gas-barrier properties for the former. This is due to the fact that during curing of solution mixed samples under high pressure the solvent molecules within the silicate inter layers favor the motion of the intercalated IIR chains [41]. By reinforcing IIR with swollen clay platelets, Liang et al. introduced a new method of composite fabrication [42]. Samadi and Kashani [43] observed cloisite10A as the most efficient reinforcing clay for butyl-rubber compounds and the same is used in this work. Maiti et al. [44] succeeded in dispersing filler in rubber via radical grafting reaction [44]. Grafting of IIR with maleic anhydride (MA) can introduce polar groups on the non polar IIR backbone, which improves the IIR/organoclay compatibility depending on the grafting level [45, 46]. Makoto et al. [35] performed solvent assisted MA grafting on IIR, whereas Gunberg and Ridgewood [47] employed a solvent-free method.

Up to now, many researchers worked on IIR/clay nanocomposites, but none of them could achieve much improvement in the mechanical and barrier properties simultaneously. In the present work, for the first time, we compare the interfaces of IIR compounds filled with the two widely used two dimensional fillers, cloisite10A and thermally reduced graphene (TRG). Secondly, the influence of MA grafting on the cloisite 10A–rubber interface is evaluated by carefully comparing the samples with different MA-grafted poly(isobutylene-*co*-isoprene) (MA-g-IIR) content. MA-g-IIR was used along with IIR to improve the dispersion of clays in the prepared composites. Morphological evidence was obtained from FTIR, SEM, AFM, XRD and TEM techniques and correlated with the filler and elastomer interactions existing at the composite interfaces. Finally the mechanical and gas permeability properties of clay and graphene composites were compared and both properties are found to be respectively depending on the filler–filler and filler–elastomer interactions in the composites.

Experimental procedure

Materials

IIR was purchased from Exxon Company and the nanoclay, Cloisite10A (density 1.90 g/cm^3) was obtained from Southern Clay Products. Natural flake graphite, MA, curing agents, benzoyl peroxide, xylene and all other minor reagents were purchased from Aldrich, France.

Preparation of TRG from GO

Graphene is prepared from graphite by following chemical approach. This technique involves two key steps: (1) oxidation of graphite to GO and (2) thermal reduction of the prepared GO to TRG. Firstly, GO is prepared by the so-called improved GO synthesis method [48]. For the reduction of GO, the thermal method was preferred rather than chemical method [49, 50] so that better dispersion is achieved with TRG. For thermal reduction, nitrogen gas was passed through GO for 30 min in sealed container to create an inert atmosphere on GO surface and the resulting product was placed in pre-heated muffle furnace at 1,000 °C for 30 s.

Preparation of MA-g-IIR

MA-g-IIR was prepared according to the method described by Makoto et al. [35] method. First, 100 g of IIR and 42 g of MA were dissolved in 400 ml xylene at 110 °C. Benzoyl peroxide (1.86 g) was dissolved in 100 ml xylene and delivered drop wise into the IIR solution over a period of 10 min. The IIR solution was stirred at 110 °C for 3 h, and then poured into acetone, resulting in the precipitation of MA-g-IIR. The MA-g-IIR was dried at 80 °C in a vacuum oven till it attained a constant weight. Using the size exclusion chromatographic technique the molecular weights of IIR and MA-g-IIR were determined and is given in Table 1. Grafting is confirmed on the basis of the decrease in molecular weight observed for MA-g-IIR.

Preparation of nanocomposites

Solution mixing process was employed for synthesizing IIR nanocomposites in order to get better dispersion cloisite10A and graphene in IIR. A constant filler loading of 5 phr is used for all samples. At first, filler was sonicated in THF for 1 h and then mixed with IIR and or MA-g-IIR/THF solution using mechanical stirrer for 3 h. All composites were dried at 80 °C in a vacuum oven till it attained a constant weight. The cured samples were obtained by mixing the nanocomposites with the curing agents such as stearic acid at 2 phr, zinc oxide (Activator) at 5 phr, 2-bisbenzothiazole-2, 2′-disulfide (MBTS) at 0.5 phr, tetramethyl thiuram disulfide (TMTD) at 1 phr and sulfur (elemental sulfur S_8) at 1.5 phr, in an internal brabender mixer at 20 rpm and at 50 °C for 30 min. The samples were cured by press molding at 160 °C for their optimum cure times determined from the Moving Die Rheometer. The composition of the prepared samples is listed in Table 2.

Table 1 Molecular weight of poly(isobutylene-*co*-isoprene) and maleic anhydride grafted poly(isobutylene-*co*-isoprene) from size-exclusion chromatography (SEC)

Samples	M_w (g/mol)×10^5	M_n (g/mol)×10^5	M_w/M_n
IIR	5.1	2.9	1.75
MA-g-IIR (0.75 %)	2.9	1.4	2.03

Solvent used for analysis is THF

Characterization

The mechanical measurements were carried out in an INSTRON 5566A universal tensile machine at a test speed of 10 mm/min. Dog bone-shaped samples were used for the tests and the measurements were done at room temperature (25 °C). The stress relaxation was monitored for a constant strain of 40 % for all the measurements for 2 h with 100 mm/min rate to attain the required strain. XRD measurements were carried out in an expert model of Philips diffractometer with Cu $K_{\acute{a}}$ radiation generator (1.5404 Å, 40 kV, 40 mA). The ultra-thin transmission electron microscopy (TEM) samples of 70-nm thickness were cut using a cryogenic ultramicrotome Leica ultracut UCT at −90 °C and images were taken using a JEOL JEM-1400 electron microscope at 100 kV. Scanning electron microscopic images of the cryo cut samples were taken with JEOL JSM-6460LV SEM. Atomic force microscopy (AFM) images were recorded with diCaliber Veeco Instrument. In order to measure the molecular weights, a Shimadzu SP 10Avp UV dual wavelength detector (λ_1=254 nm and λ_2=280 nm) was used with THF solvent at room temperature. The oxygen transmission rate (OTR) across the material is monitored using an oxysence 400B device. Payne effect was observed from the strain sweep experiments from 0.01 % to 10 % at a frequency of 0.5 Hz using Metravib dynamic mechanical analyser.

Results and discussions

FTIR analysis and the grafting degree

It is established that the increase in the grafting density for polymers results in decrease in the molecular weight [37]. The rate of chain scission depends on concentration of benzoyl peroxide, temperature, reaction time, etc. The decrease in molecular weight observed for MA-g-IIR from the GPC data (Table 1) is because of the free radical induced chain scission of IIR by benzoyl peroxide during grafting. In addition to the GPC technique, FTIR spectroscopy gives confirmation for the MA grafting on IIR.

Figure 1 shows the FTIR spectra of raw IIR and MA-g-IIR. Contrasted to the FTIR of raw IIR, the appearance of new absorbance peaks at 1,860 and 1,785 cm^{-1} (corresponding to two $V_{C=O}$ vibrational stretching modes,

Table 2 Data of compounding, poly(isobutylene-*co*-isoprene) (IIR), maleic anhydride grafted poly(isobutylene-*co*-isoprene) (MA-g-IIR)

Sample codes	Composition (Phr)			
	IIR	MA-g-IIR	Cloisite10A	TRG
IIR	100	0	0	–
RC=IIR (100 phr)+Cloisite10A (5 phr)	100	0	5	–
M2=IIR (80 phr)+MA-g-IIR (20 phr)+Cloisite10A (5 phr)	80	20	5	–
M4=IIR (60 phr)+(40 phr)+Cloisite10A (5 phr)	60	40	5	–
M6=IIR (40 phr)+MA-g-IIR (60 phr)+Cloisite10A (5 phr)	40	60	5	–
M8=IIR (20 phr)+MA-g-IIR (80 phr)+Cloisite10A (5 phr)	20	80	5	–
MC=MA-g-IIR (100 phr)+Cloisite10A (5 phr)	0	100	5	–
RG=IIR (100 phr)+Thermally reduced graphene (5 phr)	100	–	–	5

symmetric and asymmetric in MA) in MA-g-IIR indicate the MA grafting onto the IIR backbone. FTIR is also used for determining the grafting degree following Tosaka et al. [51] method. The peaks located at 1,780 and 2,728 cm^{-1} (Fig. 1) can be assigned to the stretched vibration absorbance of the carbonyl and methyl groups, respectively. Since the methyl groups on the IIR were unaffected during grafting, the ratio of the absorbance at 1,780 cm^{-1} over that at 2,728 cm^{-1} ($A_{1,780}/A_{2,728}$) was taken as a measure of the relative grafting degree. It is observed that the level of grafting depends on the experimental conditions (temperature, MA content, etc.). The grafting time was determined to be 3 h since this yields acceptable grafting level and chain scission degrees. The grafting density of 0.75 % is found as the best and was chosen for the future experiments.

Morphology of graphene and nanocomposites

The thickness of GO was determined by AFM and after thermal reduction, graphene sheets were characterized by XRD. Figure 2 demonstrates the AFM images which indicate the thicknesses of the exfoliated GO layers to be ~1.5 nm while width and length are in the range of ~1 μm. The XRD

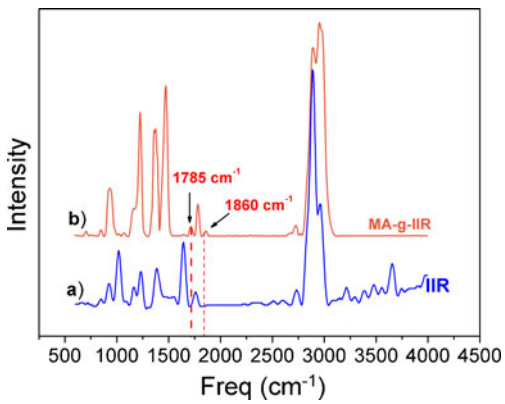

Fig. 1 FT-IR spectra of **a** neat poly(isobutylene-*co*-isoprene) (*IIR*) and **b** maleic anhydrate grafted poly(isobutylene-*co*-isoprene) (*MA-g-IIR*)

patterns of natural graphite (NG), IIR, IIR/TRG (RG) (Table 2) nanocomposites are presented in Fig. 3a. The XRD of TRG shows no characteristic peak, indicating its complete exfoliation. The appearance of a broad peak at 15° in Fig. 3a, for IIR and IIR/RG films, is due to the amorphous phase of IIR [17]. The diffraction ascribed to NG (2θ= 26.5°) does not appear in the XRD pattern of the IIR/TRG composite, indicating the complete exfoliation of TRG in the IIR matrix.

Figure 3b shows the XRD profiles of cloisite10A, RC, M2, M4, M6, M8 and MC nanocomposites. The (001) diffraction of cloisite10A at 2θ=4.8°, corresponds to an inter-layer spacing of 1.83 nm. For the composite samples RC, M2 and M4, the characteristic (001) peak of the cloisite10A is shifted to 2θ=1.92°, corresponding to a basal spacing of 4.61 nm. The position of the (001) peak basically does not change with the improvement of MA-g-IIR content in the nanocomposite, while the peak intensity decreases significantly and peak broadness increases. M6, M8 and MC, exhibit no characteristic peak in the XRD trace because of the complete loss of regularity between the clay layers. Owing to the low molecular weight, the MA-g-IIR can easily penetrate into the agglomerated nanoplatelets, strongly interact with the platelets' edges and can start the peeling off process that yields exfoliation [52]. However, it is difficult for XRD to draw definitive conclusions about the dispersion of clay in nanocomposites. Thus, microscopic techniques such as SEM and TEM are necessary to provide an actual image of the clay layers and to permit the identification of the nanocomposites morphology. Since the resolution of SEM is not enough to picture the dispersed platelets, TEM micrographs for the RC and M6 nanocomposites are taken as given in Fig. 4.

Since clay has much higher electron density than neat polymers, it appears dark in TEM images. TEM micrograph for IIR/cloisite10A (RC) nanocomposites shows that the clay layers consist of highly multilayered stacks of about 20–100 nm (Fig. 4a). On the other hand, in the micrographs of IIR/MA-g-IIR/cloisite10A (M6) nanocomposites, there is

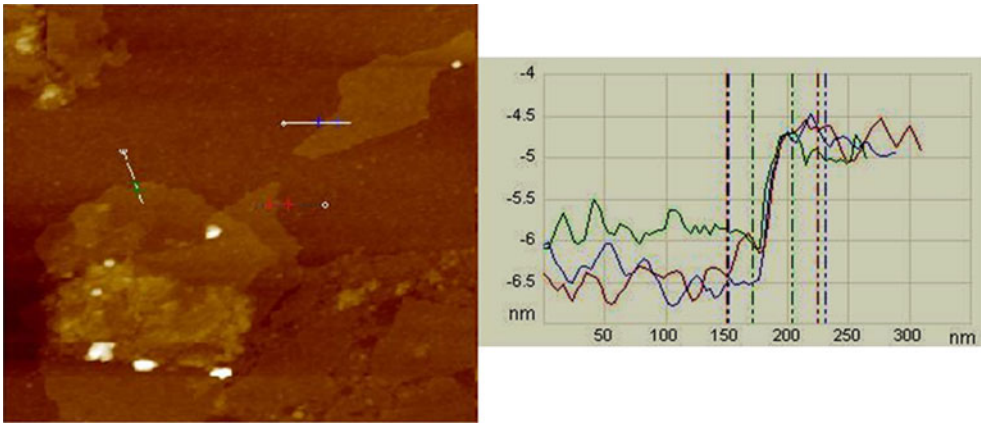

Fig. 2 AFM images of graphene oxide platelets deposited on a smooth silica surface

better dispersion of clay in the MA-g-IIR/IIR matrix (Fig. 4b). This is evidenced from the disordered single platelets observed in TEM image (Fig. 4b) which confirms the existence of a mixed intercalated/delaminated structure. The homogeneous dispersion of TRGs (Fig. 5a) in IIR is well clear from the SEM micrograph for IIR/TRG (RG) nanocomposites (Fig. 5b) itself. The floating particles (about ~0.4 μm in size) observed in the image is that of zinc oxide.

Viscoelastic behavior

Understanding the viscoelastic properties of elastomer nanocomposite is of great importance to get a fundamental knowledge of the composite microstructure. The interparticle and elastomer–filler interactions can strongly influence both linear and nonlinear viscoelastic responses [53]. Rheology is therefore an effective tool for quantifying nano filler dispersion in an uncured molten matrix. The effect of organoclay and MA-g-IIR on the apparent melt elastic modulus, G' (Pa) value of IIR is shown in Fig. 6. Comparison of the linear viscoelastic responses shows the significant effect of the clay, particularly at low frequencies (0.1–0.03 Hz). Shear rate also influences the composite morphology to a great extent. At low shear rates, the silicate platelets are well separated causing the viscosity of the melt to increase strongly, whereas shear thinning behavior is noticed at higher shear rates due to the possible orientation effect of the fillers [54].

It is observed that, at low frequencies M6, M8 and MC composites give higher G' values whereas RC behaves identically to the neat IIR matrix. M2 and M4 samples having low MA-g-IIR content also do not show significant change from the behavior of RC. The G' increase observed at low frequencies arises from the good dispersion of the platelets that increase the cohesion of the molten nanocomposites. Chemical bonds created between the MA rings of MA-g-IIR and the OH groups on the edges of the clay platelets were claimed to be at the origin of a peeling off of the clay platelets from the stacks [52]. This is consistent with the conclusion drawn by Li et al. [55] that the intensive interaction between the exfoliated silicate layers and polymer chains increases the complex viscosity and causes a marked shear thinning at low frequency values. This is pictured as well-structured M6, M8 and MC nanocomposites revealing the good dispersion of the platelets in the matrix. In the case of IIR/TRG (RG) also, the G' is much higher than the neat IIR; however this increase is not as much as observed in the case of M6. This is due to the existence of both filler–filler and filler–elastomer interactions in M6 and the presence of only the latter in RG.

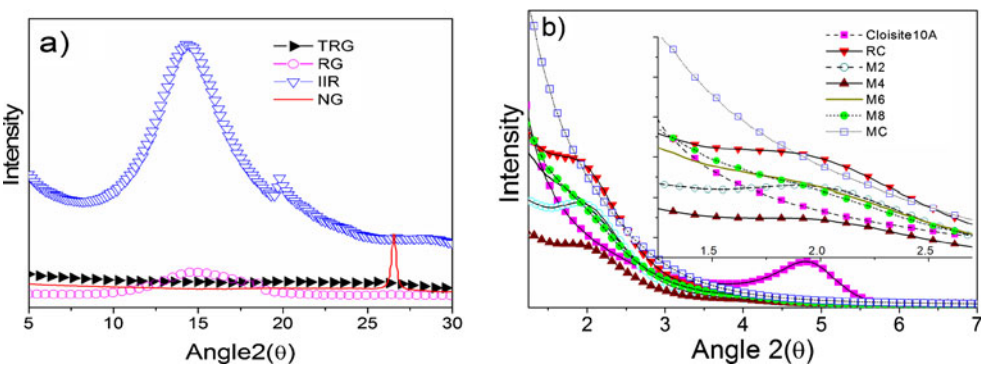

Fig. 3 WAXD patterns of **a** thermally reduced graphene (*TRG*), IIR, IIR/TRG and natural graphite (*NG*); **b** IIR/cloisite10A nanocomposites containing various amounts of MA-g-IIR

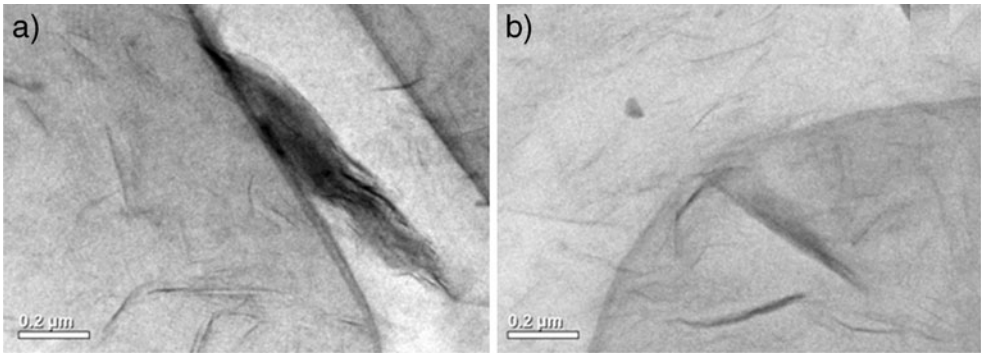

Fig. 4 TEM photographs of **a** poly(isobutylene-*co*-isoprene) (100 phr)/(5 phr) cloisite10A, (RC) and **b** poly(isobutylene-*co*-isoprene) (40 phr)+maleic anhydride grafted poly(isobutylene-*co*-isoprene) (60 phr)/(5 phr) cloisite10A, (M6)

Mechanical properties

The mechanical properties of IIR, RC (IIR/cloisite10A), M2, M4, M6, M8, MC and RG nanocomposites, quantified by tensile stress–strain measurements are summarized in Table 3 and Fig. 7. Grafting of IIR with MA improves mechanical properties of the nanocomposites due to the obtained better dispersion of cloisite10A in the matrix [45, 46] and thus the strong interface. Partial exfoliation of nano clay, depending on the grafting level was clear from TEM images. Makoto et al. [35] noticed an improvement in the barrier properties without any significant improvement in mechanical properties for the organo modified clay/MA-g-IIR nanocomposites (with very high grafting 1.75 %). In this study, we prepared a very low grafted system 0.75 %, by reducing the reaction time and simultaneously achieved significant improvement in both mechanical and permeability properties as discussed hereafter. In addition to the tensile strength, the elongation at break value is also enhanced. More clearly IIR/cloisite10A shows ~0.15 times improvement in tensile modulus compared to the unfilled matrix and it increases with the amount of MA-g-IIR up to 60 phr and then started decreasing. For tensile strength and elongation at break of M6, the increase is ~4.1 and ~2 times higher than that of the unfilled IIR. It can be observed that the dispersed nanoclay layers effectively improve the mechanical properties (strain and elongation at break) of M6 better than other composites. M6 contains sufficient amount of MA-g-IIR chains to disperse the clay and the remaining ungrafted IIR provide additional strength. Because of the higher molecular weight compared to M8 and the better dispersion of clay compared to M4, M2 and RC, the M6 is found to be the strongest IIR clay nanocomposite.

The tensile modulus (Young's modulus) of IIR/graphene is ~2.4 times higher than that of the unfilled matrix because of the strong filler–rubber interactions in RG than all other IIR/clay nanocomposites. The high specific surface area and the two-dimensional geometry of TRG result in improved mechanical interlocking and adhesion with polymeric chains [56, 57]. Xin et al. [20] reported that the GO/HXNBR composite with 0.44 vol.% of GO has a balanced mechanical properties whereas at 1.3 vol.% loading, they observed a decrease in tensile strength and an increase in Young's modulus for the GO/HXNBR composite compared to the neat HXNBR. The same conclusion is drawn for our RG system for which 5 phr level of graphene loading yields the highest modulus but not the highest strain and elongation at break when compared to clay nanocomposites which may be due to the lack of strong filler–filler interactions.

Stress relaxation

Dynamic mechanical tests can better understand the nanocomposites properties. The process of stress relaxation takes place due to both physical and chemical changes in the rubber matrix. The initial (reversible) change is caused by relaxation of the polymer chains and fillers. Long-term (irreversible) changes occur due to chemical reactions over

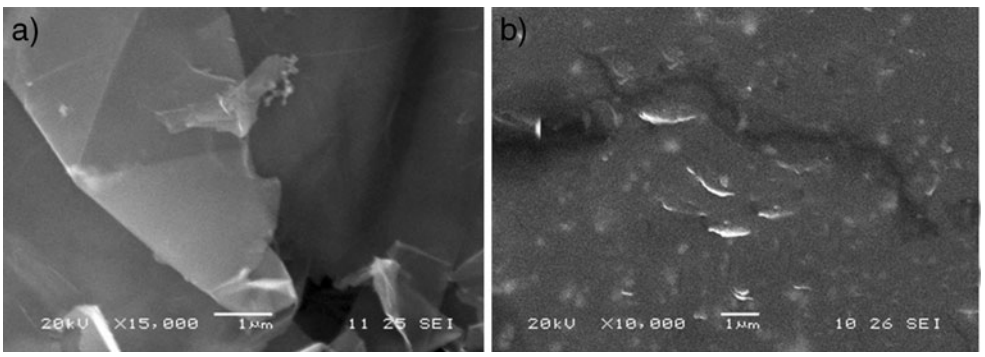

Fig. 5 SEM photographs of **a** thermally reduced graphene and **b** poly(isobutylene-*co*-isoprene) (100 phr)+thermally reduced graphene (5 phr)

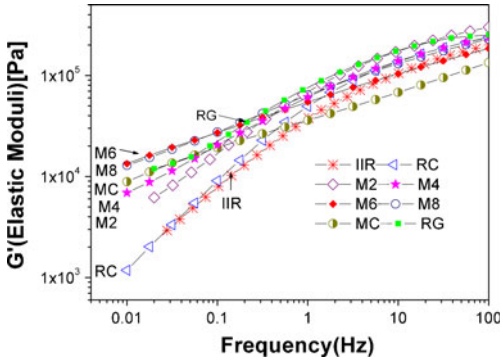

Fig. 6 Variation in elastic modulus, G' for neat IIR, IIR/cloisite10A, IIR/graphene MA-g-IIR/cloisite10A and IIR/cloisite10A nanocomposites containing various loadings of MA-g-IIR at a test strain of 1 % and at a temperature of 150 °C

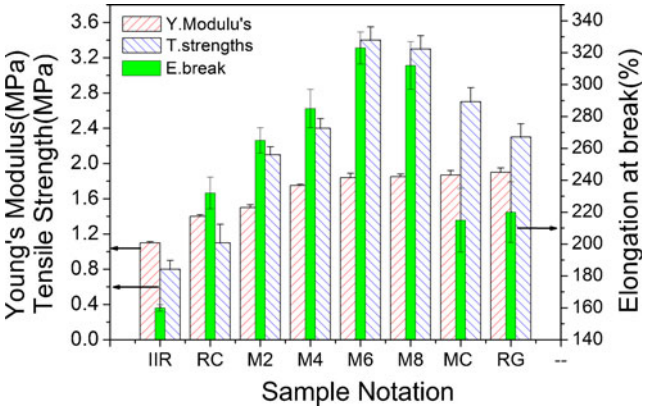

Fig. 7 Young's modulus (MPa), tensile strength (MPa) and elongation at break (%) of neat IIR, IIR/graphene, IIR/cloisite10A, MA-g-IIR/cloisite10A and IIR/cloisite10A nanocomposites containing various loadings of MA-g-IIR

time. A partial explanation of this can be provided by the theory of "strain amplification" [58] which assume greater strain in the polymer phase of a filled matrix than the overall strain due to the inextensibility of the filler. Stress relaxation rates, in general, increase with increasing polymer extension, thus filled rubbers would be expected to show higher relaxation rates [59, 60]. Other reasons for the higher relaxation rates in filled rubbers may, in some cases, are associated with filler–filler or filler–polymer interactions breakdown. The stress relaxation of polymers is attributed to chain motion and orientation, disentangling of polymer chain network strands, and deformation and rupture of micro domains and crosslinks [61]. If stress relaxation occurs, part of the energy stored in the material will be dissipated and part of deformed chains cannot retract. In the case of filled rubbers, desorption of polymer chains from the filler surface occur and the dewetting starts or propagates during the time of observation and the rate increases greatly. It was already reported that the extent of such breakdown varies with the nature of the filler [62]. To explain the observed behavior, the experimental relaxation curves of the composites were fitted to the stretched exponential Kohlrausch equation (Eq. 1) given by

$$\frac{\sigma_t}{\sigma_0} = \frac{\sigma_\infty}{\sigma_0} + \frac{\sigma_1}{\sigma_0} \exp\left[-(t/\tau)^\beta\right] \quad (1)$$

where σ_∞/σ_0, σ_t/σ_0, τ, and β are the fitting parameters. Here, τ is the relaxation time, β is the stretching parameter ($0<\beta\leq 1$), σ_∞/σ_0 is the transient stress, σ_t/σ_0 is the limiting stress and $[(\sigma_0 - \sigma_\infty)/\sigma_0] \times 100$ is the relaxation ratio. The value of σ/σ_0 is called the normalized stress and the dependence of this on time is plotted as the stress relaxation curve. The best fit for the experimental values with the parameters of Eq. 1 are given in Table 4. From the fitting parameters, the relaxation time τ, and the stretching exponent β were estimated in order to understand the mechanism of the relaxation processes in the filled rubber composites.

Figure 8 shows the stress relaxation curves [(σ_t/σ_0) vs. time, t] for the neat IIR, IIR/TRG, IIR/cloisite10A, MA-g-IIR/cloisite10A and IIR/cloisite10A nanocomposites containing various loading of MA-g-IIR at a constant elongation of

Table 3 Mechanical and Oxygen gas permeability properties of neat IIR, IIR/TRG, IIR/cloisite10A, MA-g-IIR/cloisite10A and IIR/cloisite10A nanocomposites containing various loadings of MA-g-IIR

Sample codes	Mechanical properties			OTR (ml/m^2/24 h)
	Young's modulus (MPa)	Tensile strength (MPa)	Elongation at break (%)	
IIR	0.9.±0.01	0.8±0.10	160±02	38.4±0.3
RC	1.40±0.02	1.1±0.21	232±10	35.6±0.4
M2	1.50±0.03	2.1±0.09	265±08	33.4±0.2
M4	1.75±0.02	2.4±0.11	285±12	32.6±0.3
M6	1.84±0.07	3.5±0.15	323±10	31.5±.0.2
M8	1.85±0.03	3.3±0.15	312±15	30.5±.0.3
MC	1.87±0.05	2.6±0.26	215±20	29.6±0.3
RG	1.91±0.06	2.7±0.15	220±19	28.4±0.2

Table 4 Fitting parameters of Eq. 1

Sample codes	σ_∞/σ_0	σ_1/σ_0	β	$\tau_{(min)}$	Relaxation ratio $[(\sigma_0-\sigma_\infty)/\sigma_0]\times 100$
IIR	0.8920	0.9846	0.20	0.012	12.09
RC	0.8591	0.9859	0.25	0.11	16.39
M2	0.8025	0.9327	0.20	0.20	24.60
M4	0.7397	0.9132	0.20	0.22	35.14
M6	0.6952	0.8695	0.21	0.25	41.85
M8	0.6805	0.8703	0.29	0.50	46.93
MC	0.6329	0.8286	0.25	0.56	61.03
RG	0.8085	0.9893	0.3	0.31	24.16

40 %. It is observed that the stress decays with time until it approaches an equilibrium value. To evaluate the effect of the filler–polymer interactions, the values for IIR/TRG (RG) and IIR/cloisite10A (RC) are compared. Since the reinforcing mechanisms are different for the cloisite10A and graphene filled systems, their stress relaxation behavior can be originated from different sources. For RC, the relaxation in stress can be mostly attributed to the rupture of cloisite10A–IIR interactions, whereas it is not enough for the interaction breakage in graphene–IIR system. The addition of MA-g-IIR to IIR/cloisite10A (RC) decreases the overall chain flexibility and thus leads to a slow relaxation process. The results indicate that the addition of MA-g-IIR has a very strong effect on the crosslink density of the composites due to its influence on the physical and chemical interactions of IIR and cloisite10A (in RC). According to Chih-Cheng et al. [63], the stability of rubber–rubber interaction is stronger than filler–rubber and filler–filler interactions due to the hydrogen bonds present (Fig. 8b) [64]. The increase in the MA-g-IIR content led to the increase in the relaxation time (Table 4), which is again due to the strong filler–rubber interactions. This higher degree of polymer–filler interactions is further evidenced from the higher contribution in the progressive failure in filler–rubber bonding. For IIR/TRG (RG), the stress relaxation time is lower than that of MA-g-IIR/cloisite10A (MC), even though they have good reinforcement (from Young's moduli) with rubber, but MC has strong filler–filler interaction than RG. The strong filler–rubber and filler–filler interactions are the reasons for the greater responses in the stress relaxation experiments in MC.

Payne effect

The dependence of strain on the storage moduli of nanocomposites at 25 °C is studied (Fig. 9), and the Payne effect is observed. The filled composites show obviously higher storage modulus (G') than neat rubber [65, 66]. However, the rate of MA grafting has a strong positive influence on the Payne effect due to the significant reinforcement. Since the storage modulus is related to the crosslink density for the filled composites (Eq. 2), the interactions within the composites can be deduced from storage moduli values.

$$G' = Nk_BT \tag{2}$$

where k_B is the Boltzmann constant, T is the temperature and N ($N_{total}=N_c+N_{st}+N_i$) is the crosslink density of the filled network. N_c is the chemical crosslink density and bonds from entanglement, N_{st} is the number of rubber–filler stable bonds per unit volume and N_i is the number of rubber–filler unstable bonds per volume unit of the material.

The filler–filler and filler–rubber interactions based on Payne effect (decrease in G' with increase in strain amplitude) can be explained by several models. The well-known

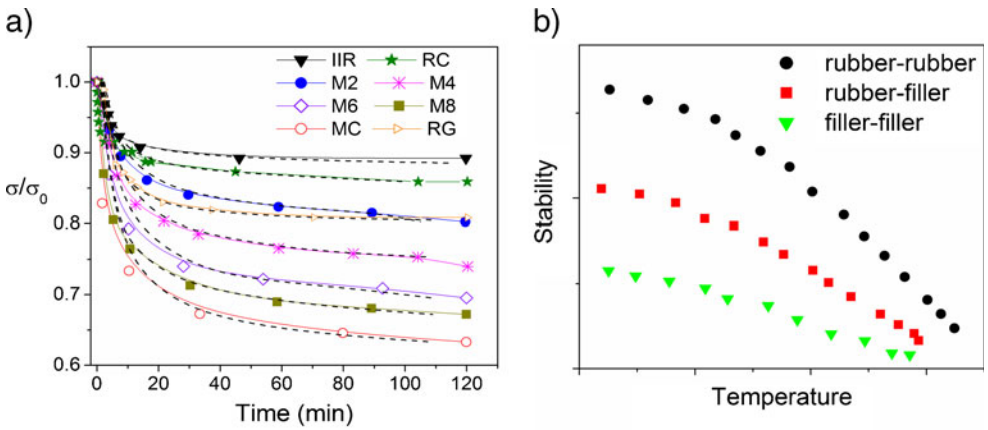

Fig. 8 **a** Stress relaxation curves, time dependence on the normalized stress for neat IIR, IIR/graphene, IIR/cloisite10A, MA-g-IIR/cloisite10A and IIR/cloisite10A nanocomposites containing various loading of MA-g-IIR. (The *dotted lines* represent the curve fits.) **b** Stability of bonds responsible [63]

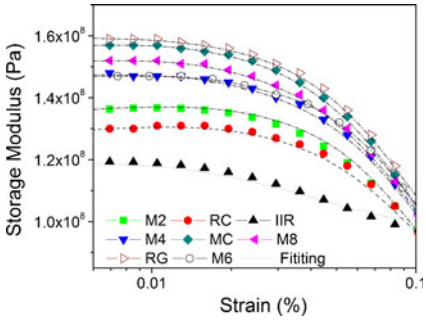

Fig. 9 Strain dependence of the storage modulus at 25 °C temperature for neat IIR, IIR/graphene, IIR/cloisite10A, MA-g-IIR/cloisite10A and IIR/cloisite10A nanocomposites containing various loading of MA-g-IIR (*dotted lines* represent the curve fits)

Maier and Göritz [64] model mainly considers filler–rubber interactions with stable (strong) and unstable (weak) filler–rubber bonds (Eq. 3). The present composite systems studied here were observed to be in good agreement with this model (Fig. 9) revealing the significance of filler–rubber interactions.

$$G'(\gamma) = G'_{st} + G'_{i}\left(\frac{1}{1+c\gamma}\right) \quad (3)$$

where $G_{st}'=(N_g+N_{st})k_BT$ and $G_i'=N_ik_BT$. G_{st}' is the value of G' at high deformations and G_I' represents the Payne amplitude.

The number of rubber–filler stable bonds per unit volume for the neat IIR and various IIR nanocomposites are calculated based on this equation and given in Table 5. The elastic modulus of the composite comes from two factors, the pure rubber contribution and the filler contribution based on the filler/rubber interface. The number of rubber–filler stable bonds per unit volume for neat IIR ($N_{st}=0.12\times10^{26}/cm^3$) is lower than all its nanocomposites due to the lack of additional cross links from the filler side. IIR/graphene (RG) shows the highest number of stable bonds ($N_{st}=3.65\times10^{26}/cm^3$) among all nanocomposites because of the strong interactions between rubber and graphene. Among the clay nanocomposites, MC has highest number of stable bonds. Figure 9 also shows the increase in the number of stable bonds with the amount of MA-g-IIR. This is attributed to the increased specific surface area with the increase in MA-g-IIR content, which can improve the number of bonds and thus the filler–rubber bond formation. The same conclusion can be drawn from the analysis of the unstable bonds as well.

Oxygen transmission rate

One of the important properties for IIR is its low gas permeability. The incorporation of layered structure nano fillers into polymer matrices has shown to be highly effective in reducing gas and solvent permeability [30–32, 42, 67]. The OTR values of IIR, RG, RC, MC, M2, M4, M6, and M8 are included in Table 3. A lower OTR is detected for RG when compared to the clay reinforced samples. By following the simple diffusion experiments using toluene and by calculating the diffusion coefficient values, the aspect ratios of the two fillers clay and graphene were estimated to be 108±8 and 130±2, respectively. The relatively higher aspect ratio of graphene in IIR matrix compared to clay platelets is one of the main reasons for the higher OTR rate in the clay sample. Factors like permeate interaction with filler and filler–polymer interactions [29–32],also affect OTR values. It has been proposed by Hailin et al. [68] that due to the poor compatibility of the silica surface and the polymer, the polymer chains could not tightly contact the silica nanoparticles, and thus it forms a narrow gap surrounding the silica particles. Indeed, graphene has more surface area (~2,630 m^2/g) than clay (~750 m^2/g) and, gas molecules need more time to cross graphene barrier than clay barrier.

Long tortuous path and high width are evidenced for IIR/TRG composite compared to the grafted and ungrafted IIR/cloisite10A composites because of the high surface area of TRGs and its better exfoliation in the elastomer medium. Well-exfoliated graphene sheets are evident from the XRD and TEM analysis. In fact the larger aspect ratio of graphene sheets (130±2) over the clay (108±8) leads to higher surface area and thus the better dispersion of graphene in IIR.

Table 5 Fitting parameters of Eq. 3

Sample codes	G_{st}' ($10^6\times$Pa)	G_i' ($10^8\times$Pa)	N_{i0} ($10^{28}\times cm^{-3}$)	N_g+N_{st} ($10^{26}\times cm^{-3}$)	c
IIR	0.05	1.16	2.06	0.122	3
RC	1.10	1.36	3.31	2.43	4
M2	1.15	1.48	3.60	2.80	4.3
M4	1.20	1.53	3.72	2.92	4.0
M6	1.40	1.55	3.77	3.40	4.2
M8	1.45	1.56	3.77	3.52	3.5
MC	1.50	1.61	3.91	3.62	4.4
RG	1.56	1.67	4.06	3.65	4.9

All these point out towards the improved barrier property of RG. Among the cloisite10A composites, MC exhibit lower gas permeability than all others because of nanometer level dispersion of cloisite10A. In between M8 and M6, the former exhibit the same level of gas permeability of MC. But in the case of M6, the well dispersion (from XRD and TEM) and strong interface causes difficulty for the gas molecules to pass through the tightly crosslinked system [68, 69] compared to RC, M2 and M4, thus making MC a mechanically strong impermeable membrane. The orientation of platelets strongly depends on the barrier properties of composites as explained by Bharadwaj model [26]. But here, the same level of orientation is assumed for all composites due to the exactly similar preparation techniques and only the nature of fillers and filler polymer interactions are addressed in order to explain the permeability.

Even though the properties of clay and graphene filler reinforced composites are compared in this work, both these fillers are different in their aspect ratios, nature and interactions with the polymer chains. The correlation of molecular interactions occurring inside the composites and the more focused permeability application makes this study very meaningful.

Conclusions

The role of fillers like graphene and cloisite10A as well as the influence of grafting was studied in the IIR rubber matrix for a better understanding of the nano filler dispersion, interactions, mechanism of reinforcement and oxygen diffusion. We highlighted the possibility of tuning the grafting level to obtain MA-g-IIR/IIR ratio that maximizes rubber–filler interactions and act as physical crosslinking for the 60 phr MA-g-IIR/cloisite10A system. Very good level of filler dispersion is observed at 5 phr level, which is maintained throughout the study. Young's modulus, Stress relaxation and Payne effect values are found to be enhanced for MA-g-IIR/IIR/cloisite10A composites. Due to the high aspect ratio and good filler–polymer interactions, the graphene nanocomposites exhibit a good enhancement in Young's, storage modulus and decrease in oxygen permeability. The remarkably improved impermeability of IIR/graphene nanocomposites compared with the optimized IIR/cloisite10A nanocomposites arises also from the high specific surface area of graphene that hinder oxygen diffusion. Thus, the composite properties are successfully correlated with the filler elastomer molecular interactions taking place in IIR composites depending on the degree of grafting and nature of filler as well as the composition of composites. In the future experiments we are trying to find the synergistic effect of clay and graphene to improve the mechanical and permeability of rubber simultaneously.

Acknowledgments The authors acknowledge the French Ministry for Research and the Brittany Region and the Department of Science and Technology, India, for the financial support. We also thank the Nanofunc Program of the Pays de la Loire Region for helping in the TEM analysis.

References

1. Kamigaito O, Fukushima Y, Doi H (1984) Composite material composed of clay mineral and organic high polymer and method for producing the same. US patent 4,472,538
2. Kojima Y, Usuki A, Kawasumi M, Okada A, Fukushima Y, Kurauchi T, Kamigaito O (1993) Mechanical properties of nylon 6-clay hybrid. J Mater Res 8:1185–1189
3. Kojima Y, Usuki A, Kawasumi M, Okada A, Kurauchi T, Kamigaito O (1993) Sorption of water in nylon 6–clay hybrid. J Appl Polym Sci 49:1259–1264
4. Van Olphen H (1977) An introduction to clay colloid chemistry, 2nd edn. Wiley, New York
5. LeBaron P, Wang Z, Pinnavaia T (1999) Polymer-layered silicate nanocomposites: an overview. Appl Clay Sci 15:11–29
6. Vaia RA, Price G, Ruth PN, Nguyen HT, Lichtenhan J (1999) Polymer/layers silicate nanocomposites as high performance ablative material. Appl Clay Sci 15:67–92
7. Kim J, Oh T, Lee D (2003) Morphology and rheological properties of nanocomposites based on nitrile rubber and organophilic layered silicates. Polym Int 52:1203–1208
8. Kim J, Oh T, Lee D (2003) Preparation and characteristics of nitrile rubber (NBR) nanocomposites based on organophilic layered clay. Polym Int 52(7):1058–1063
9. Zhang H, Zhang Y, Peng Z, Zhang Y (2004) Influence of clay modification on the structure and mechanical properties of EPDM/montmorillonite nanocomposites. Polym Test 23:217–223
10. Gatos KG, Sawanis NS, Apostolov AA, Thomann R, Karger-Kocsis J (2004) Nanocomposite formation in hydrogenated nitrile rubber (HNBR)/organo-montmorillonite as a function of the intercalant type. Macromol Mater Eng 289:1079–1086
11. Schon F, Thomanm R, Gronski W (2002) Shear controlled morphology of rubber/organoclay nanocomposites and dynamic mechanical analysis. Macromol Symp 189(1):105–110
12. Gatos KG, Thomanm R, Karger-Kocsis J (2004) Characteristics of ethylenepropylene diene monomer rubber/organoclay nanocomposites resulting from different processing conditions and formulations. Polym Int 53:1191–1197
13. Zhang H, Zhang Y, Peng Z, Zhang Y (2004) Influence of the caly modification and compatibilizer on the structure and mechanical properties of ethtlene–propylene–diene rubber/montmorillonite composites. J Appl Polym Sci 92(1):638–646
14. Sengupta R, Chakraborty S, Bandyopadhyay S, Dasgupta S, Mukhopadhyay R, Auddy K, Deuri AS (2007) A short review on rubber/clay nanocomposites with emphasis on mechanical properties. Polym Eng Sci 47(11):1956–1974
15. Yanhu Z, Jinkui W, Hesheng X, Ning Y, Guoxia F, Guiping Y (2011) Dispersion and exfoliation of graphene in rubber by an ultrasonically-assisted latex mixing and in situ reduction process. Macromol Mater Eng 296(7):590–602
16. Meneghetti P, Qutubuddin S (2006) Synthesis, thermal properties and applications of polymer-clay nanocomposites. Thermochem Acta 442:74–77
17. Huiqin L, Shuxin L, Kelong L, Liangrui X, Kuisheng W, Wenli G (2011) Study on modified graphene/butylrubber nanocomposites: I. Preparation and characterization. Polym Eng Sci 51(11):2254–2260

18. Song SH, Jeong HK, Kang YG (2010) Preparation and characterization of exfoliated graphite and its styrene butadiene rubber nanocomposites. J Ind Eng Chem 16:1059–1065
19. Prud'Homme R, Ozbas B, Aksay I, Register R, Douglas A (2010) Functional graphene rubber nanocomposites. US patent 7,745,528 B2
20. Xin B, Chaoying W, Yong Z, Yinghao Z (2011) Reinforcement of hydrogenated carboxylatednitrile–butadiene rubber with exfoliated graphene oxide. Carbon 49:1608–1613
21. Chen D, Tang L, Li J (2010) Graphene-based materials in electrochemistry. J Chem Soc Rev 39:3157–3180
22. Park S, Ruoff RS (2009) Chemical methods for the production of graphenes. Nat Nanotechnol 4:217–224
23. Geim AK, Novoselov KS (2007) The rise of graphene. Nat Mater 6:183–191
24. Rafiee MA, Rafiee J, Wang Z, Song H, Yu ZZ, Koratkar N (2009) Enhanced mechanical properties of nanocomposites at low graphene content. ACS Nano 3:3884–3890
25. Owen CC, Soyoung K, Cynthia P, John MT, SonBinh TN (2010) Crumpled graphene nanosheets as highly effective barrier property enhancers. Adv Mater 22:4759–4763
26. Bharadwaj RK (2001) Modelling the barrier properties of polymer-layered silicate nanocomposites. Macromolecules 34:9189–9192
27. Cussler EL, Hughes SE, Ward WJ, Aris R (1988) Barrier membranes. J Membr Sci 38:161–174
28. Nielsen LE (1967) Models for the permeability of filled polymer systems. J Macromol Sci 5:929–942
29. Stephen R, Varghese S, Joseph K, Oommen Z, Thomas S (2006) Diffusion and transport through nanocomposites of natural rubber (NR), carboxylated styrene butadiene rubber (XSBR) and their blends. J Membr Sci 282:162
30. Meera AP, Thomas SP, Thomas S (2012) Effect of organoclay on the gas barrier properties of natural rubber nanocomposites. Polym Compos 33:524–531
31. Saritha A, Joseph K, Thomas S, Muraleekrishnan R (2012) The role of surfactant type and modifier concentration in tailoring the properties of chlorobutyl rubber/organo clay nanocomposites. J Appl Polym Sci 124:4590–4597
32. Saritha A, Joseph K, Thomas S, Muraleekrishnan R (2012) Chlorobutyl rubber nanocomposites as effective gas and VOC barrier materials. Compos A Appl Sci Manuf 43:864–870
33. Hofmann W (1989) Rubber technology handbook, 2nd edn. Hanser Publishers, New York
34. Qu L, Huang G, Wu J, Tang Z (2007) Damping mechanism of chlorobutyl rubber and phenolic resin vulcanized blends. J Mater Sci 42:7256–7262
35. Makoto K, Azusa T, Hiromitsu T, Amritsu U, Isamu I (2006) Preparation and properties of isobutylene–isoprene rubber–clay nanocomposites. J Polym Sci A Polym Chem 44:1182–1188
36. Liang Y, Ma J, Lu Y, Wu Y, Zhang L, Mai Y (2005) Effects of heat and pressure on intercalation structures of isobutylene/isoprene rubber clay nanocomposites. J Polym Sci B Polym Phys 43:2653–2664
37. Sridhar V, Tripathy DK (2006) Barrier properties of chlorobutyl nanoclay composites. J Appl Polym Sci 101:3630–3637
38. Ranimol S, Ranaganathaiah C, Siby V, Kuruvilla J, Thomas S (2006) Gas transport through nano and micro composites of natural rubber (NR) and their blends with carboxylated styrene butadiene rubber (XSBR) latex membranes. Polymer 47:858–870
39. Takahashi S, Goldberg HA, Feeney CA, Karim DP, Farrell M, O'Leary K, Paul DR (2006) Gas barrier properties of butyl rubber/vermiculite nanocomposite coatings. Polymer 47:3083–3093
40. Gatos G, Százdi L, Pukánszky B, Karger-Kocsis J (2005) Controlling the deintercalation in hydrogenated nitrile rubber (HNBR)/organo-montmorillonite nanocomposites by curing with peroxide. Macromol Rapid Commun 26:915–919
41. Liang YR, Wang YQ, Wu YP, Lu YL, Zhang HF, Zhang LQ (2005) Preparationand properties of isobutylene –isoprene (IIR)/clay nanocomposites. Polym Test 24:12–17
42. Yurong L, Weiliang C, Zhao L, Yiqing W, Youping W, Liqun Z (2008) A new strategy to improve the gas barrier property ofisobutylene–isoprene rubber/clay nanocomposites. Polym Test 27:270–276
43. Samadi A, Kashani MR (2010) Effects of organo-clay modifier on physical–mechanical properties of butyl-based rubber nanocomposites. J Appl Polym Sci 116:2101–2109
44. Maiti M, Sadhu S, Bhowmick AK (2005) Effect of carbon black on properties of rubber nanocomposites. J Appl Polym Sci 96:443–451
45. Salahuddin N, Akelah A (2002) Synthesis and characterization of poly(styrene-maleic anhydride)–montmorillonite nanocomposite. Polym Adv Technol 13:339–345
46. Li XC, Ha CS (2003) Nanostructure of EVA/organoclay nanocomposites: effects of kinds of organoclays and grafting of maleic anhydride on to EVA. J Appl Polym Sci 87(12):1901–1909
47. Gunberg PF, Ridgewood NJ (1958) Maleic anhydride modified butyl rubber. US Patent 2,845,403
48. Daniela CM, Dmitry VK, Jacob MB, Alexander S, Zhengzong S, Alexander S, Lawrence BA, Wei L, James MT (2010) Improved synthesis of graphene oxide. ACS Nano 4(8):4806–4814
49. Schniepp HC, Li JL, McAllister MJ, Sai H, Herrera-Alonso M, Adamson DH, Prud'homme RK, Car R, Saville DA, Aksay IA (2006) Functionalized single graphene sheets derived from splitting graphite oxide. J Phys Chem B 110:8535–8539
50. McAllister MJ, Li JL, Adamson DH, Schniepp HC, Abdala AA, Liu J, Herrera-Alonso M, Milius DL, Car R, Prud'homme RK, Aksay IA (2007) Single sheet functionalized graphene by oxidation and thermal expansion of graphite. Chem Mater 19:4396–4404
51. Tosaka M, Kawakami D, Senoo K, Kohjiya S, Ikeda Y, Toki S, Hsiao BS (2006) Crystallization and stress relaxation in highly stretched samples of natural rubber and its synthetic analogue. Macromolecules 39:5100–5105
52. Fordiani F, Aubry T, Grohens Y (2009) Structural changes evidenced by rheology in PP-g-MA nanocomposites during oxidative ageing. J Appl Polym Sci 114(6):4011–4019
53. Heinrich G, Klüppel M (2002) Recent advances in the theory of filler networking in elastomers. Adv Polym Sci 160:1–44
54. Okamoto M (2006) Recent advances in polymer/layered silicate nanocomposites: an overview from science to technology. Mater Sci Technol 22(7):756–779
55. Li J, Zhou C, Wang G, Yu W, Tao Y, Liu Q (2003) Preparation and linear rheological behavior of polypropylene–montmorillonite nanocomposites. Polym Compos 24:323–331
56. Rafiee MA, Rafiee J, Srivastava I, Wang Z, Song H, Yu ZZ, Koratkar N (2010) Fracture and fatigue in graphene nanocomposites. Small 6:179–183
57. Ramanathan T, Abdala AA, Stankovich S, Dikin DA, Herrera-Alonso M, Piner RD, Adamson DH, Schniepp HC, Chen X, Ruoff RS (2008) Functionalized graphene sheets for polymer nanocomposites. Nat Nanotechnol 3:327–331
58. Mullins L, Tobinn R (1954) Theoretical model for the elastic behaviour of filler-reinforced vulcanised rubbers. Proc. 3rd Rubber Technology Conference 397–412
59. Asaletha R, Bindu P, Aravind I, Meera AP, Valsaraj SV, Yang W, Thomas S (2008) Stress-relaxation behavior of natural rubber/polystyrene and natural rubber/polystyrene/natural rubber-graft-polystyrene blends. J Appl Polym Sci 108(2):904
60. Meera AP, Said S, Grohens Y, Luyt AS, Thomas S (2009) Tensile stress relaxation studies of TiO_2 and nanosilica filled natural rubber composites. Ind Eng Chem Res 48:3410
61. Jyotishkumar P, Pionteck J, Hassler R, George SM, Cvelbar U, Thomas S (2011) Studies on stress relaxation and thermomechanical

properties of poly(acrylonitrile-butadiene-styrene) modified epoxy–amine systems. Ind Eng Chem Res 50(8):4432–4440
62. Andrews E (1963) Reinforcing of rubber by fillers. Rubber Chem Technol 36:325–336
63. Chih-Cheng P, Gopfert A, Drechsler M, Abetz V (2005) "Smart" silica–rubber nanocomposites in virtue of hydrogen bonding interaction. Polym Adv Technol 16:770
64. Maier PG, Göritz D (1996) Molecular interpretation on the Payne effect. Kautsch Gummi Kunstst 49:18
65. Meera AP, Said S, Grohens Y, Thomas S (2009) Nonlinear visco-elastic behavior of silica-filled natural rubber nanocomposites. J Phys Chem C 113:17997
66. Bhattacharyya S, Sinturel C, Bahloul O, Thomas S, Salvetat J (2008) Improving reinforcement of natural rubber by networking of activated carbon nanotubes. Carbon 46(7):1037
67. Nilson LE, Landel RF (1994) Mechanical properties of polymers and composites, 2nd edn. Marcel Dekker, New York
68. Hailin C, Maciej R, Brian FT, Youqing S (2007) Polymer–inorganic nanocomposite membranes for gas separation. Sep Purif Technol 55:281–291
69. Soney CG, Ninan KN, Sabu T (2001) Permeation of nitrogen and oxygen gases through styrene–butadiene rubber, natural rubber and styrene–butadiene rubber/natural rubber blend membranes. Eur Polym J 37:183–191